Pulse Shaping: The Missing Piece of Backscatter Radio and RFID

John Kimionis, *Student Member, IEEE*, and Manos M. Tentzeris, *Fellow, IEEE*

***Abstract*— The increasing use of backscatter radio for pervasive Internet-of-Things systems as a low-power and low-cost communication scheme will result in dense deployments of tags that need to operate under bandwidth (BW) constraints. Typical backscatter tags and computational radio frequency (RF) identification systems are unnecessarily limited to modulating data with "ON–OFF" switching front-ends, which leads to extensive spectrum occupancy, due to the rectangular pulses. This paper sets the foundations to overcome these limitations and proposes designs of RF front-ends that are capable of varying the tag reflection coefficient in a continuous way over time. Arbitrary waveforms can be generated to perform pulse shaping on the backscattered signals, which require significantly reduced BW. The principles presented in this paper will enable sophisticated tags to perform complex modulation schemes under BW constraints, while maintaining a very low RF front-end complexity, using a single nonlinear component such as a p-i-n diode or field-effect transistor. Migrating the idea of pulse shaping from complex power-demanding active radios to such minimal RF front-ends will complete backscatter radio as a communication scheme for simple RF tags and sensors in large-scale deployments. Each tag becomes a miniature software-defined radio that implements diverse communication schemes with increased spectral efficiency.**

***Index Terms*— Backscatter radio, modulation, pulse shaping, radio frequency (RF) front-end, RF identification (RFID), software-defined radio (SDR), spectral efficiency.**

I. Introduction

IN DENSE backscatter sensor or radio frequency identification (RFID) tag deployments, minimizing the utilized bandwidth (BW) per tag is required to fit a large number of sensors in a dedicated frequency band and also guarantee low out-of-band interference for regulatory reasons. Each tag's backscattered signal spectrum has to decay fast with regard to frequency so that the signal's harmonics are suppressed and do not interfere with nearby sensors, without compromising the signal detection performance. Active radio systems typically utilize pulse shaping techniques to modify the waveform characteristics of the transmitted signals and adapt them according to the requirements of BW, data rate, and so on [1], [2]. Although conventional radio utilizes complex electronic components to achieve shaping, backscatter radio typically utilizes minimal RF front-ends consisting of only one or a few nonlinear devices (switches, transistors, and diodes) that switch between discrete states [3]. However, this should not be a strongly limiting factor for getting away from conventional ON–OFF keying (OOK) modulation on sophisticated sensing RFID tags that already employ computational units, such as microcontroller units (MCUs), at the core of their system. Examples of such computation-enabled tags include: 1) [4] where an MCU-based tag is built that implements the Gen2 industrial RFID protocol [5]; 2) [6], [7] where MCU-based tags are built to implement custom backscatter communication schemes including OOK and frequency-shift keying (FSK) in nonconventional long-range bistatic architectures presented in [8] and [9]; 3) [10] where MCU-based tags are used in a special case of bistatic architecture named ambient backscatter; 4) [11], [12] where tags are built that exploit multiple load values and RF multiplexers to achieve high-order modulation constellations; and 5) [13] where an MCU tag is operating in harmonic mode to backscatter data at the second harmonic of the reader signal. All these examples utilize rectangular pulses for backscatter communication and thus require extended BW.

The work in [14] first demonstrated the feasibility of generating nonrectangular waveforms with a backscatter tag RF front-end comprising a single nonlinear component, by exploiting a continuous variation of the antenna load instead of switching between two discrete values, as in typical backscatter/RFID tags. Appropriate nonlinear components include diodes, field-effect transistors (FETs), and any other components that feature a voltage-controlled or current-controlled impedance characteristic. Such components are widely used and are available in either discrete semiconductor packages, or they can be implemented on integrated circuit (IC) dies [15].

Although other works in the field of backscatter radio/RFID have included components that are capable of varying impedance, they have not exploited the characteristic of continuous load modulation; instead, they have limited the operation to discrete states and rectangular pulses. Examples include [16], where p-i-n diodes have been utilized for communication, and [17], where photo diodes have been utilized for sensing. In the first example, the p-i-n diodes are biased with discrete current levels for a certain duration (symbol period), and therefore the backscatter pulses have a rectangular

Manuscript received July 1, 2016; revised October 10, 2016; accepted October 25, 2016. Date of publication November 23, 2016; date of current version December 7, 2016. This work was supported in part by the National Science Foundation-EFRI and in part by the Defense Threat Reduction Agency (DTRA). An earlier version of this paper was presented at the IEEE MTT-S International Microwave Symposium, San Francisco, CA, USA, May 22–27, 2016.

The authors are with the School of Electrical and Computer Engineering, Georgia Institute of Technology, Atlanta, GA 30332 USA (e-mail: ikimionis@gatech.edu; etentze@ece.gatech.edu).

Color versions of one or more of the figures in this paper are available online at http://ieeexplore.ieee.org.

Digital Object Identifier 10.1109/TMTT.2016.2623703

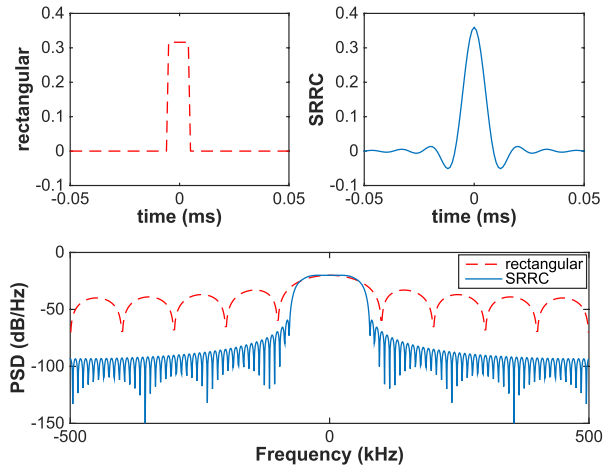

Fig. 1. Spectrum comparison of 100-kbit/s rectangular pulses (typically used in backscatter radio) and SRRC pulses of the same energy. Using pulse shaping for backscatter radio significantly reduces the required BW per RFID tag or backscatter sensor.

shape with increased BW occupancy. Moreover, due to the architecture of the circuit, only a small portion of the Smith chart can be utilized for the antenna load, significantly limiting the backscattered signal-to-noise ratio (SNR). In the second example, a sensor utilizes a photo diode as the antenna load and detection is based on the differential radar cross section (RCS) of the sensor. The differential RCS is calculated from two distinct load states, i.e., that sensor also backscatters rectangular pulses. In contrast with prior art, this work's mechanisms allow for backscattering of arbitrary signals and significantly reduced BW occupancy (Fig. 1). This will greatly benefit sensor/RFID deployments, in terms of the following.

1) *Regulatory Limitations:* Out-of-band emissions are suppressed with pulse shaping, and thus this paper facilitates tag designs that conform to spectrum regulations.
2) *Network Density:* Reduced BW per node has a direct impact on the number of nodes in the sensor/RFID network.
3) *Communication Scheme Flexibility:* Generating and backscattering arbitrary waveforms enable the use of diverse communication schemes, data rates, modulation formats, and increased spectral efficiency.
4) *Lower Complexity Readers:* Readers require significantly lower sampling rate at the receiver chain, since the reduced backscatter signal BW affects the minimum required sampling rate (Nyquist rate).

This paper is an extensive presentation of the concepts behind backscatter pulse shaping and arbitrary signal generation, the mechanisms and the front-end implementations, the processing required, as well as the power constraints of utilizing minimal simple RF front-ends. Although these front-ends consist of a single active component, they can effectively break the limitations of rectangular waveforms and high BW occupancy found in conventional RFID. Theory, simulations, and proof-of-concept front-end implementations and characterizations are offered with lab setups. Moreover, to showcase the practicality of the proposed designs on low-cost sensor nodes, the system is implemented on commodity microcontroller platforms.

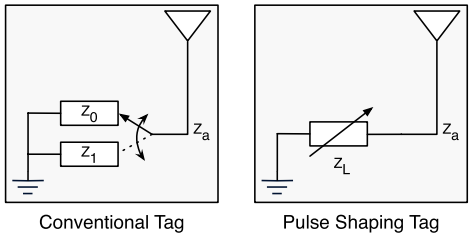

Fig. 2. Left: conventional tag switching between two discrete impedance loads. Right: pulse shaping tag with variable impedance load.

Despite these platforms' low computational ability, this work's mechanisms are successfully demonstrated to be fully operational, opening a new direction for low-power sensors and computational RFID. This paper offers a *missing piece* to make backscatter radio a *complete* communication scheme, while maintaining an extremely lower energy footprint compared with active radio.

II. Signal Model

The antenna-load system reflection coefficient for a backscatter modulator is [18], [19]

$$\Gamma = \frac{Z_L - Z_a^*}{Z_L + Z_a} \tag{1}$$

where Z_L and Z_a are the load and antenna impedance, respectively. From [9], the received complex baseband signal at the reader has the form

$$y_{\mathrm{BB}}(t) = a_{\mathrm{dc}} e^{j\phi_{\mathrm{dc}}} + a_{\mathrm{mod}} e^{j\phi_{\mathrm{mod}}} \Gamma(t-\tau). \tag{2}$$

The term $a_{\mathrm{dc}} e^{j\phi_{\mathrm{dc}}}, a_{\mathrm{dc}} \in \mathbb{R}, \phi_{\mathrm{dc}} \in [0, 2\pi)$ corresponds to the compound unmodulated (dc) components of the received signal, i.e., the reader-emitted carrier continuous wave (CW) and the tag's unmodulated structural scattering. The term $a_{\mathrm{mod}} e^{j\phi_{\mathrm{mod}}}$ scales the received modulated tag signal by $a_{\mathrm{mod}} \in \mathbb{R}$ and rotates it on the complex plane by a phase $\phi_{\mathrm{mod}} \in [0, 2\pi)$. The terms $a_{\mathrm{dc}} e^{j\phi_{\mathrm{dc}}}$ and $a_{\mathrm{mod}} e^{j\phi_{\mathrm{mod}}}$ also include the impact of a static/quasi-static environment, i.e., channel attenuation and multipath effects. The tag signal is a direct function of Γ over time, delayed by a time constant τ that depends on the wireless channel propagation. Note that all amplitude and phase terms are unknown at the reader, and the received baseband signal after timing recovery $y_{\mathrm{BB}}(t+\tau)$ is equal to the tag-modulated signal $\Gamma(t)$ after unknown offsetting, scaling, and rotation on the complex plane.

Backscatter modulation is achieved when $\Gamma(t)$ changes over time, due to changes of the modulator's load impedance $Z_L(t)$ over time. Typically, backscatter load modulators utilize two load values for $Z_L(t)$ to achieve binary communication [Fig. 2(left)]. In that case, the baseband received signal $y_{\mathrm{BB}}(t)$ features sharp changes between two values, i.e., the waveform consists of rectangular pulses. Note that the two distinct received levels are, in general, complex. To transmit data at a data rate $R = 1/T$, where T is the bit duration, a very large BW W (infinite in theory) is required in the frequency domain, since the Fourier transform of a rectangular pulse in time domain is a sinc in frequency domain (Fig. 1).

However, according to the Nyquist intersymbol interference (ISI) criterion in communication theory, the required BW could be minimized to $W = R$ while maintaining reliable communication without ISI, which negatively affects bit detection [1]. A pulse typically used in active radio transceivers with limited BW is the square root raised cosine (SRRC) pulse, which, at the expense of longer pulse duration, features a significantly reduced mainlobe BW [20]. The SRRC extends from $t_1 = -AT$ to $t_2 = AT$, where A is the *filter delay*, in contrary to a rectangular pulse that extends from $t_1 = -T/2$ to $t_2 = T/2$ [e.g., compare the pulse duration of a rectangular pulse and an SRRC pulse with $A = 5$ in Fig. 1(top)]. This reduces the required pulse BW [1] to

$$W = \frac{1+a}{T} \tag{3}$$

where $0 \leq a \leq 1$ is the roll-off factor that defines how fast the pulse spectrum decays in the frequency domain. The difference in spectrum occupancy for rectangular and SRRC pulses of the same energy is apparent in Fig. 1(bottom), where the power spectral density (PSD) of the two pulses is shown. Moreover, when using SRRC filters at the receiver to match filter incoming SRRC pulses, the result is a raised cosine pulse, which satisfies the Nyquist ISI criterion, i.e., it is ISI free, which increases the bit detection performance. Therefore, it is appealing to be able to generate SRRC pulses or other arbitrary waveforms with smooth envelopes (e.g., Gaussian pulses [1]) with a simple backscatter front-end to significantly suppress the signal spectral sidelobes, or generate multilevel waveforms to achieve amplitude modulation schemes such as M-ary pulse amplitude modulation, or generate arbitrary waveforms for other modulation schemes (e.g., sinusoids for analog frequency modulation or digital FSK). As discussed in the following sections, this can be achieved without the need of high-complexity electronics, but rather with a single active element front-end that continuously varies the antenna load in a continuous way.

III. Continuous Load Variation

The principles described in this section can be applied to any antenna that is complex-valued or real-valued, as well as any varying load that is complex-valued or real-valued, according to the general form of (1). However, without loss of generality, and to make the quantities easy to visualize, a purely resistive load $Z_L = R(V_{\text{bias}})$ controlled by a bias voltage V_{bias} and an antenna impedance $Z_a = 50\ \Omega$ are assumed. Then the antenna-load reflection coefficient is

$$\Gamma(V_{\text{bias}}) = \frac{R(V_{\text{bias}}) - 50}{R(V_{\text{bias}}) + 50}. \tag{4}$$

and it is a real quantity with $1 \geq \Gamma(V_{\text{bias}}) \geq -1$. Let V_{min} be a low voltage level for which $\Gamma(V_{\text{min}}) = 1$, i.e., the antenna load acts as an open circuit ($R \to \infty$). Similarly, let V_{max} be the voltage level that turns the load to a short circuit ($R = 0\ \Omega$), i.e., the reflection coefficient is $\Gamma(V_{\text{max}}) = -1$. Moreover, let V_0 be the voltage that minimizes the reflection coefficient magnitude $|\Gamma(V_0)| = 0$, which occurs at $R = 50\ \Omega$.

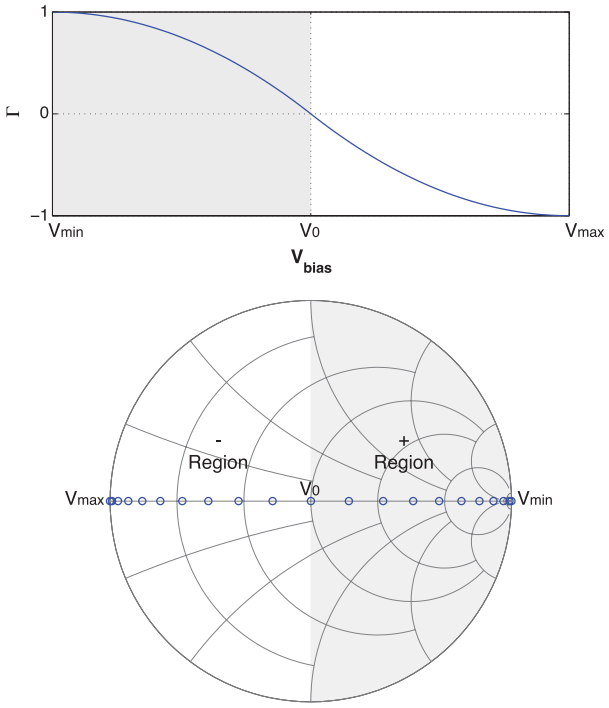

Fig. 3. Reflection coefficient of (4) as a function of bias voltage in linear form and impedance representation.

The reflection coefficient as a function of the bias voltage is shown in Fig. 3 in linear scale and on a Smith chart, where it can be seen that reflection coefficient variations close to the edges of the Smith chart (high return loss) are more "dense," in contrast with the ones close to the chart's center, for equidistant variations of the bias voltage. The gray regions of the linear graph and the Smith chart correspond to positive reflected signals, and the white regions correspond to negative reflected signals. Assuming an incident RF signal to the load, a positive or negative voltage of any level between -1 and $+1$ can be reflected back by applying the appropriate bias value.[2]

The reflection coefficient can be decomposed to its magnitude and phase components as shown in Fig. 4. It can be seen that the reflection coefficient values can be split into one "positive" region and one "negative" region. Note that the point of sharp transition in phase coincides with the point where the reflection coefficient amplitude is minimized. This decomposition is useful because even if there is a phase rotation of $\Gamma(V_{\text{bias}})$, the amplitude function will remain the same, and the two regions can still be defined, since they will have opposite signs. The breakpoint can be found by

$$V_0 = \arg\min_{V_{\text{bias}}} |\Gamma(V_{\text{bias}})|. \tag{5}$$

Then the positive region will be the $\Gamma(V_{\text{bias}})$ values for which $V_{\text{bias}} < V_0$, and the negative region will be the $\Gamma(V_{\text{bias}})$ values

[1]" BW " here refers to the RF spectrum BW around the modulation carrier (e.g., 900 MHz). The equivalent baseband spectrum would extend from dc to $(1+a)/(2T)$ Hz.

[2]The work in [21] has offered designs that backscatter signals with reflection coefficient values $|\Gamma| > 1$. Those designs involve negative-resistance loads to amplify-and-reflect incident signals; this paper assumes passive loads only, confined within the unitary circle of the Smith chart.

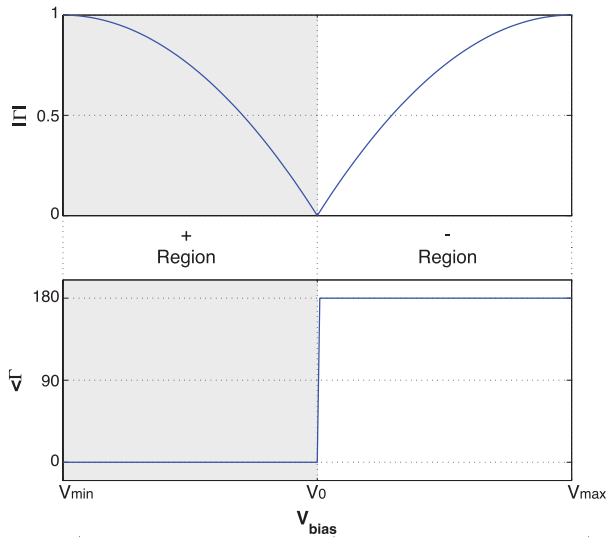

Fig. 4. Reflection coefficient of (4) decomposed to magnitude and phase components, defining a positive and a negative reflected signal region.

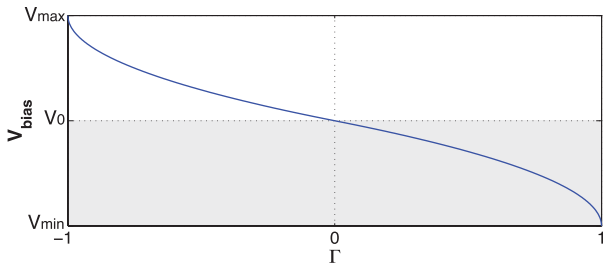

Fig. 5. Inverted function of (6) providing the required bias voltage to achieve a certain reflection coefficient value.

for which $V_{\text{bias}} > V_0$. Even if the definition of the positive and negative values is inverted, it does not alter the pulse shaping principle, since the opposite phase will just contribute an extra π radians in the already-unknown phase at the receiver [ϕ_{mod} in (2)]. After this decomposition, it becomes apparent that any signal level (from 0 to 1) can be generated with two possible signs, making it possible to generate arbitrary waveforms.

To generate an arbitrary signal, the required bias voltage to yield the corresponding reflection coefficient is needed. This involves inverting the function $\Gamma(V_{\text{bias}})$, i.e., finding the function

$$V_{\text{bias}}(\Gamma), \text{ for which: } \Gamma(V_{\text{bias}}(\Gamma)) \equiv \Gamma(V_{\text{bias}}). \tag{6}$$

Note that V_{bias} and Γ denote scalar values, while $V_{\text{bias}}(\cdot)$ and $\Gamma(\cdot)$ denote scalar functions. From Fig. 3(top), it can be seen that $\Gamma(V_{\text{bias}})$ is a 1–1 function, and thus invertible; the inverse $V_{\text{bias}}(\Gamma)$ function is shown in Fig. 5.

Assume we need to transmit an arbitrary pulse $x(t)$, e.g., the one shown in Fig. 6(left). The amplitude level of the pulse is first confined in the interval $[-1, 1]$ with the normalization

$$\tilde{x}(t) = \frac{x(t)}{\max|x(t)|} \tag{7}$$

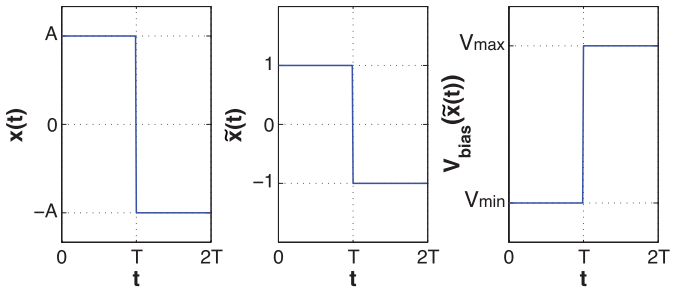

Fig. 6. Left: pulse to be transmitted. Center: transformation to reflection coefficient values [applying (7)]. Right: transformation to required bias voltage [applying (8)].

to yield the pulse shown in Fig. 6(center), which is expressed in reflection coefficient-domain values (-1 to 1). Using the $V_{\text{bias}}(\Gamma)$ function in Fig. 5, $\tilde{x}(t)$ can be translated to the bias voltage required to yield this reflection coefficient variation over time. The result is the bias voltage function over time

$$V_{\text{bias}}(\tilde{x}(t)) = V_{\text{bias}}(\Gamma)|_{\Gamma=\tilde{x}(t)} \tag{8}$$

shown in Fig. 6(right).

IV. Pulse-Shaping Front-End Design

Two front-end designs are presented, one comprising a p-i-n diode and one comprising a FET transistor switch. Both components have a voltage-controlled resistance behavior, and their impedance varies in a continuous way, instead of sharply transitioning between two values, thus making them ideal for pulse shaping front-end design. However, pulse shaping front-ends could be implemented with *any* nonlinear element or elements that show a controlled impedance behavior, not necessarily limited to voltage-controlled resistance. Moreover, in Section VIII, more options for pulse shaping front-ends are discussed, involving analog *RLC* filters. All presented front-ends try to exploit the full range of impedance values on the Smith chart so that they maximize the backscattered signal energy and increase the detection performance at the reader. However, this implies that at the beginning or end of every symbol, the modulator is always in a reflective state, which is challenging for RF tags that employ harvesters for powering and/or energy storage. The work in [22] has offered solutions for hybrid three-state front-ends that can accommodate RF harvesters along with modulators that are fully reflective for uncompromised communication. The concepts of that work can be applied in conjunction with the pulse shaping modulators presented in this section.

A. p-i-n Diode Front-End

A first choice for a front-end with a single active element that features a voltage-controlled resistance behavior is a diode. Specifically, a p-i-n diode (Skyworks SMP1302-079LF) targeted to variable attenuator applications is essentially an RF-thru with S_{21} attenuation that depends on the applied bias voltage.

The p-i-n diode is terminated to a short circuit to achieve maximum reflection with a negative sign $\Gamma_{\text{short}} = -1$ when

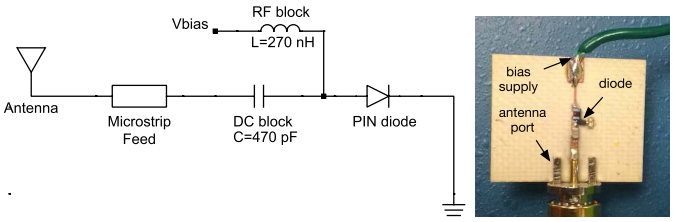

Fig. 7. Pulse shaping front-end schematic (left) and prototype (right).

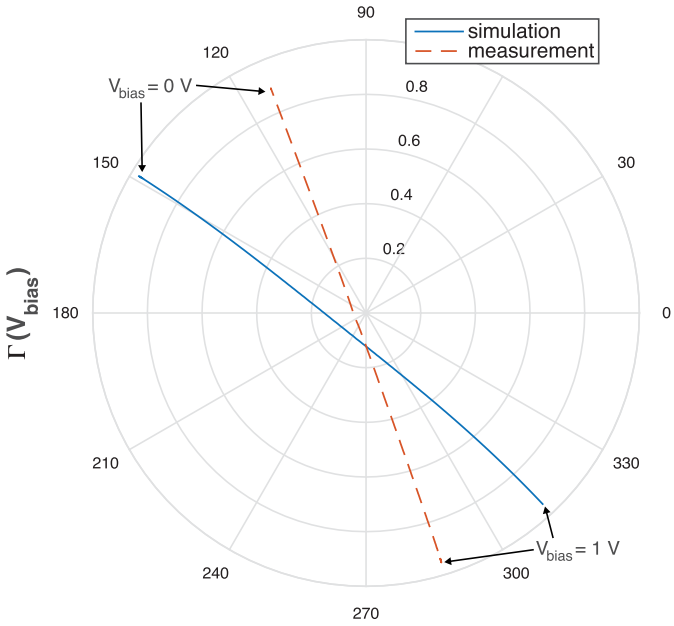

Fig. 8. Reflection coefficient versus bias voltage level (0–1 V) for p-i-n diode front-end (913 MHz).

the p-i-n diode is fully biased and maximum reflection with a positive sign when the diode is not biased and behaves as an RF open $\Gamma_{\text{open}} = 1$. A dc bias network is connected to the diode's anode with an RF-block inductor in the bias voltage path and a dc-block capacitor in the RF path [Fig. 7(left)]. The front-end is analyzed with Keysight advanced design system utilizing a nonlinear SPICE model for the diode, manufacturer models for the lumped components, and full-wave simulation of the PCB layout and the feeding microstrip line. The simulated $\Gamma(V_{\text{bias}})$ is shown in Fig. 8. Compared with the theoretical plot of Fig. 3, the curve shows a phase shift and a small offset from the center of the polar plot, due to: 1) the phase introduced by the microstrip feeding line and 2) parasitics of the p-i-n diode. These practically do not affect the received signal at the reader, since the offset will contribute to the unmodulated dc term of (2), and the phase shift will be absorbed by the already-present phase term $e^{j\phi_{\text{mod}}}$ that rotates $\Gamma(t-\tau)$ on the complex plane.

The front-end is implemented on a double copper-clad Rogers RO4003C laminate with a dielectric constant $\epsilon_r = 3.55$, loss tangent $\tan\delta = 0.0021$, and substrate thickness 20 mil [Fig. 7(right)] and is characterized using an automated setup of continuous bias voltage sweeping with a voltage source and S-parameter measurements with a vector network analyzer (Fig. 9). The measured reflection coefficient for a bias

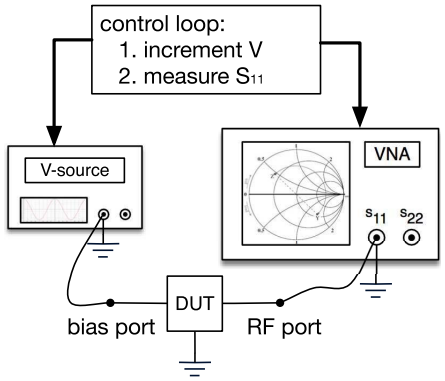

Fig. 9. Front-end characterization setup.

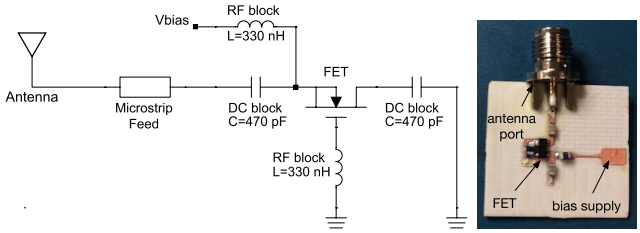

Fig. 10. FET implementation of pulse shaping front-end schematic (left) and prototype (right).

voltage range of 0–1 V features a similar behavior with the simulated data (Fig. 8), with an introduced phase shift (due to the phase introduced by the SMA connector), which, as mentioned previously, does not affect the signal detection at the reader.

B. FET Switch Front-End

A similar attenuation mechanism is also implemented with a FET, since it features a drain–source resistance variation that depends on the gate voltage. A front-end has been built with an RF FET (NXP BF1118), which primarily targets switching applications and has been used in previous works as a switch for binary backscatter modulation by biasing to a low or a high voltage level [22], [23]. However, when sub-biased, the FET switch acts as a voltage-controlled variable impedance and can be used for pulse shaping, since the source–drain resistance changes with the gate–source voltage (Fig. 10).

An n-channel depletion-type MOSFET terminated with a short is used as a variable-attenuation thru line. Since the transistor is biased with negative gate–source (V_{GS}) voltage levels, the gate is grounded ($V_G = 0$) and the bias voltage is applied to the FET's source ($V_S = V_{\text{bias}}$). Apart from the dc-block capacitor and RF-block inductor used for the biasing network, an extra dc-block capacitor is used between the FET's drain and the ground short, to prevent dc current flow from the source to the ground when the source–drain channel is 'ON.' The capacitor value is high (470 pF) so that it still acts as an RF-short, not affecting the front-end's pulse shaping operation.

The FET front-end is implemented on RO4003C laminate and characterized with the measurement setup in Fig. 9. The measured $\Gamma(V_{\text{bias}})$ is shown in Fig. 11 for voltage levels from 0 to 2 V. It can be seen that a continuous variation of

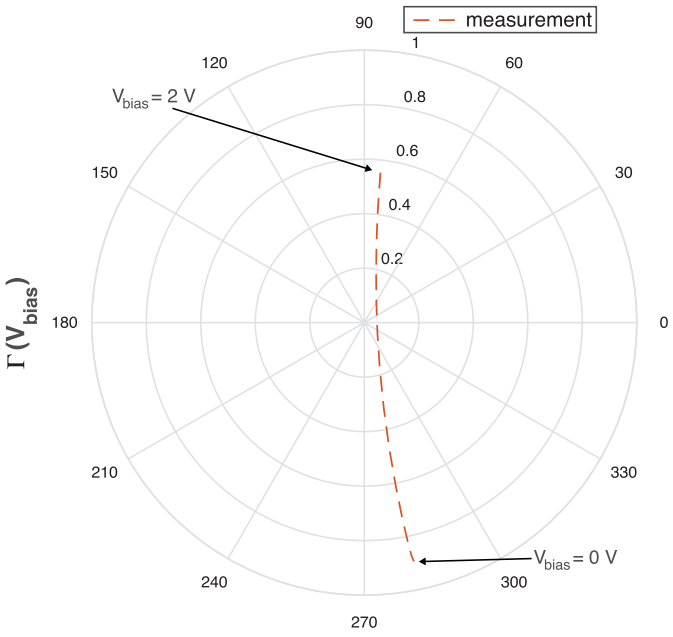

Fig. 11. Reflection coefficient versus bias voltage level (0–2 V) for FET front-end (913 MHz).

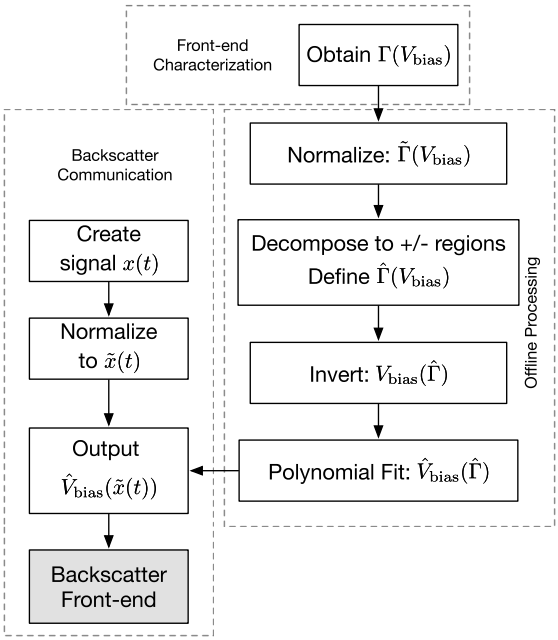

Fig. 12. Characterization, processing, and communication steps.

the reflection coefficient is achieved when changing the bias voltage, although the reflection coefficient variation does not cover the whole Smith chart from end to end. This is due to the insertion loss of the FET switch at the "ON" state, and will affect the backscattered signal in terms of lower reflected power. Although there is an offset from the center of the polar plot, a scaling, and a phase shift, these do not affect the signal demodulation at the reader, and proper processing steps shown in Section V can guarantee the exploitation of the full range of reflection coefficient values. Also, the effect of the small curvature close to the value $V_{\text{bias}} = 0$ will be negligible as shown in Section V.

V. Processing and Measurements

The steps required to use a pulse shaping-capable front-end for arbitrary signal generation are summarized in Fig. 12. After characterizing a pulse shaping-capable front-end with the setup in Fig. 9, the $\Gamma(V_{\text{bias}})$ function has been obtained and a series of offline processing steps is required that need to be run once. This is also facilitated by the fact that there is a very small variation of the reflection coefficient values for the UHF band from 850 to 950 MHz. Fig. 13 shows the measured Γ values for both front-ends in the two edge cases of 0/1 V for the p-i-n and 0/2 V for the FET. The calculated standard deviation is between 0.028 and 0.05 for all cases within 850–950 MHZ, which makes the front-ends suitable for broadband operation in the whole UHF band. Within the 900–928-MHz RFID band, the deviation is between 0.008 and 0.015 for all cases. The result of the offline processing is used by the backscatter communicator to transmit pulse-shaped signals.

A. Offline Processing

The following processing steps are intended to be run offline after the front-end characterization. They involve calculations

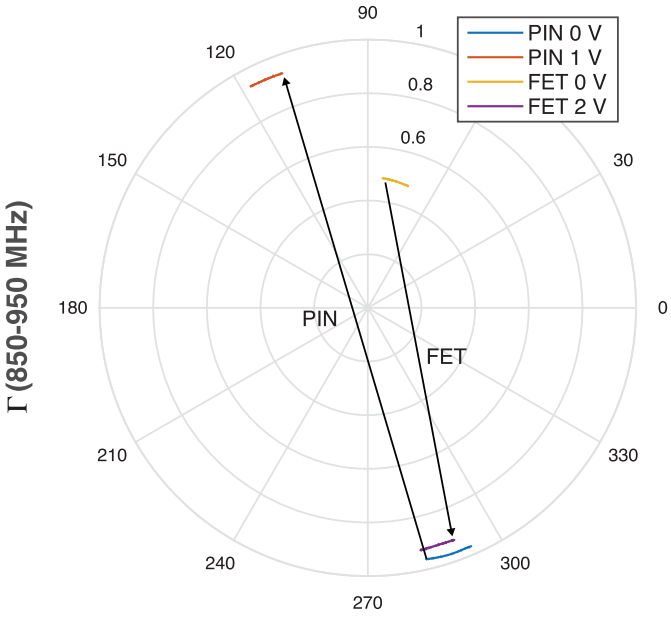

Fig. 13. Measured reflection coefficient variation across 850–950-MHz band for p-i-n and FET front-ends.

that would take part on a computer, and the individual steps are straightforward to implement in MATLAB or other software. It is noted that the steps need to be run once, assuming negligible behavior differences of the nonlinear components due to manufacturer tolerances and variations.

1) Normalization: The measured $\Gamma(V_{\text{bias}})$ function for actual front-end implementations will differ from the function shown in Fig. 3, as it is going to be affected by offsetting, scaling, and rotation. That means that for an ideal function $\Gamma_{\text{ideal}}(t)$ that has the form of Fig. 3 and extends from -1 to 1, an actual front-end function $\Gamma(t)$ has the form

$$\Gamma(t) = s\ \Gamma_{\text{ideal}}(t) + c \tag{9}$$

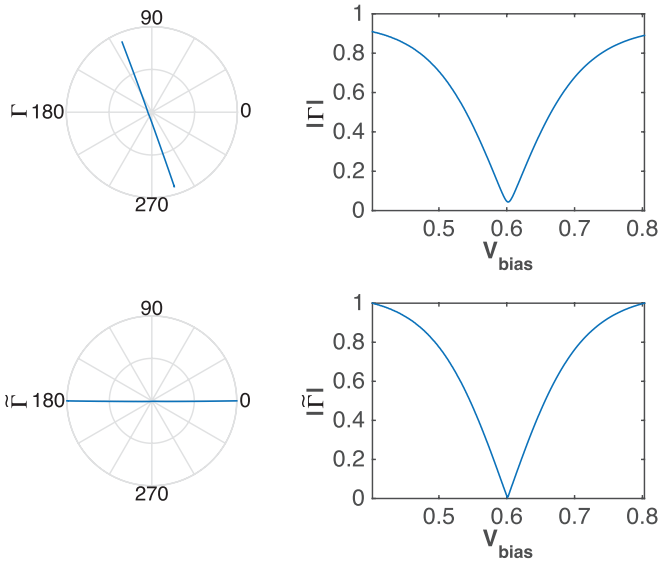

Fig. 14. Normalization of reflection coefficient values. Measured data from p-i-n diode used for processing.

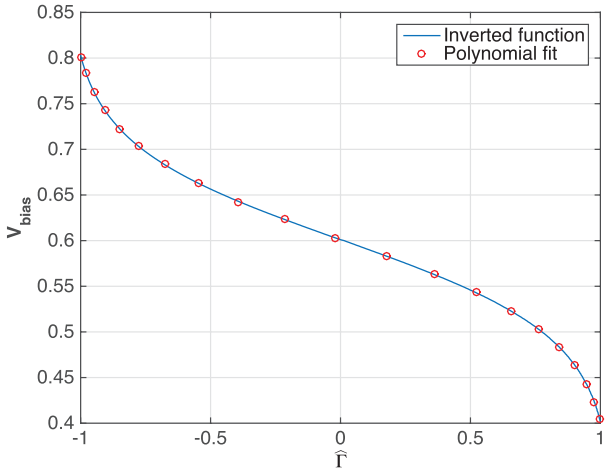

Fig. 15. Inverted $V_{\text{bias}}(\hat{\Gamma})$ function and polynomial-fitted $\hat{V}_{\text{bias}}(\hat{\Gamma})$ points. Measured data from p-i-n diode are used for processing.

where $s, c \in \mathbb{C}$, i.e., the scaling factor s will scale down and rotate the $\Gamma_{\text{ideal}}(t)$ function on the complex plane, and the offset factor c will move the scaled-and-rotated function $s\Gamma_{\text{ideal}}(t)$ toward *any* direction on the complex plane. For such a function, the baseband received signal at the reader will be

$$\begin{aligned} y_{\text{BB}}(t) &= a_{\text{dc}}e^{j\phi_{\text{dc}}} + a_{\text{mod}}e^{j\phi_{\text{mod}}}\Gamma(t-\tau) \\ &= a_{\text{dc}}e^{j\phi_{\text{dc}}} + a_{\text{mod}}e^{j\phi_{\text{mod}}}(s\ \Gamma_{\text{ideal}}(t-\tau)+c) \\ &= a'_{\text{dc}}e^{j\phi'_{\text{dc}}} + a'_{\text{mod}}e^{j\phi'_{\text{mod}}}\Gamma_{\text{ideal}}(t-\tau) \end{aligned} \tag{10}$$

where $a'_{\text{dc}}e^{j\phi'_{\text{dc}}} = a_{\text{dc}}e^{j\phi_{\text{dc}}} + c\ a_{\text{mod}}e^{j\phi_{\text{mod}}}$ is the new compound unmodulated dc term and $a'_{\text{mod}}e^{j\phi'_{\text{mod}}} = s\ a_{\text{mod}}e^{j\phi_{\text{mod}}}$ is the scaling and rotating term of the modulated signal $\Gamma_{\text{ideal}}(t-\tau)$. The signal of (10) is of the same form with (2), since the dc terms and scaling terms are unknown at the reader. Therefore, any offset, scaling, or rotation of the reflection coefficient does not affect the reader processing.

Since offsetting, scaling, and rotation do not affect reader processing, it is convenient to normalize the measured reflection coefficient values to the form of Fig. 3 so that the subsequent steps treat reflection coefficient functions for any front-end in the same way. The normalization operation is

$$\tilde{\Gamma}(V_{\text{bias}}) = \frac{\Gamma - \hat{c}}{\hat{s}} \triangleq \frac{\hat{s}^*\Gamma(V_{\text{bias}}) - \hat{s}^*\hat{c}}{|\hat{s}|^2} \tag{11}$$

where $\hat{c}$ is the offset factor estimate

$$\hat{c} = \frac{\Gamma(V_{\max}) + \Gamma(V_{\min})}{2} \tag{12}$$

$\hat{s}$ is the scaling factor estimate

$$\hat{s} = \frac{\Gamma(V_{\max}) - \Gamma(V_{\min})}{2} \tag{13}$$

and $\hat{s}^*$ is the complex conjugate of $\hat{s}$. In Fig. 14(top), the measured reflection coefficient values of the p-i-n front-end can be seen for bias voltages from 0.4 to 0.82 V. The reason for truncating the 0–1 V measurements' interval to 0.4–0.82 V is that practically any voltage level between 0 and 0.4 V yields $\Gamma = 0.9$ and any level between 0.82 and 1 V practically yields $\Gamma = -0.9$. In Fig. 14(bottom), the normalized reflection coefficient values for the same voltage interval can be seen. Note how the polar plot and the magnitude of the reflection coefficient are of the same form with the theoretical plots (Figs. 3 and 4).

2) Decomposition to Positive and Negative Regions: As discussed in Section III, the reflection coefficient function is decomposed to a positive and a negative region. This involves estimating the breakpoint

$$\hat{V}_0 = \arg\min_{V_{\text{bias}}} |\tilde{\Gamma}(V_{\text{bias}})| \tag{14}$$

and then defining the function

$$\hat{\Gamma}(V_{\text{bias}}) = \begin{cases} |\tilde{\Gamma}(V_{\text{bias}})|, & V_{\text{bias}} \le \hat{V}_0 \\ -|\tilde{\Gamma}(V_{\text{bias}})|, & V_{\text{bias}} > \hat{V}_0. \end{cases} \tag{15}$$

3) Function Inversion: The function $\hat{\Gamma}(V_{\text{bias}})$ with the two positive/negative regions is 1–1 and is inverted to obtain $V_{\text{bias}}(\hat{\Gamma})$, which can be used as a lookup function to translate signals in reflection coefficient-domain values (in $[-1,\ 1]$) to corresponding bias voltage levels.

4) Polynomial Fitting: A polynomial fitting step follows, which describes function $V_{\text{bias}}(\hat{\Gamma})$ with a small number of coefficients, and smooths out signal discontinuities and measurement noise. The coefficients can be used to store the function in a low-memory device such as an MCU for later evaluation, or evaluate the function in predefined steps of $\hat{\Gamma}$ and store the resulting values in a lookup table. In Fig. 15, the inverted function $V_{\text{bias}}(\hat{\Gamma})$ is plotted along with its evaluated polynomial-fit function $\hat{V}_{\text{bias}}(\hat{\Gamma})$.

B. Backscatter Communicator

The steps associated with the backscatter communication (Fig. 12) are intended to run real time on a tag that either generates bits based on dynamic information (e.g., sensor data) or recalls static bits from its memory (e.g., identification data). The following steps are intended to run in a loop.

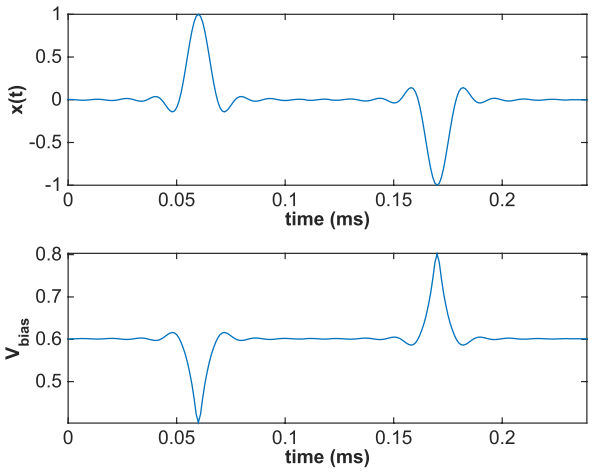

Fig. 16. Two SRRC pulses (one positive and one negative) in reflection coefficient and bias voltage representation. Measured data from p-i-n diode are used for processing.

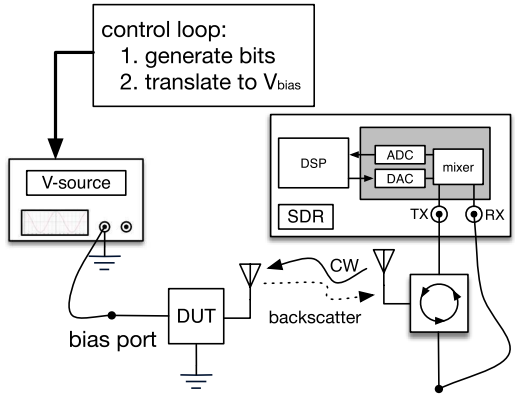

Fig. 17. Front-end measurement setup.

1) Signal Creation: The communicator is generating an arbitrary signal $x(t)$ for transmission, e.g., a positive and a negative SRRC pulse in Fig. 16(top).

2) Normalization: The signal $x(t)$ is normalized to $\tilde{x}(t)$ according to (7), to constrain it to reflection coefficient-domain values, from -1 to 1.

3) Voltage Output: The fitted function $\hat{V}_{\text{bias}}(\hat{\Gamma})$ is used to translate the signal $\tilde{x}(t)$ to the required voltage levels. This can be done by evaluating a N-degree polynomial with

$$\hat{V}_{\text{bias}}(\tilde{x}) = p_N \tilde{x}^N + p_{N-1}\tilde{x}^{N-1} + \cdots + p_1 \tilde{x} + p_0 \quad (16)$$

where p_n, $n \in N$ are the fitted polynomial coefficients obtained during the offline processing step B-4 . The signal $\hat{V}_{\text{bias}}(\tilde{x}(t))$ is output to bias the pulse shaping RF front-end. Fig. 16(bottom) shows the bias voltage levels required to backscatter the pulses of Fig. 16(top).

VI. Pulse Shaping Measurements

To test the pulse shaping front-ends, the experimental setup in Fig. 17 has been utilized, consisting of a full-duplex software-defined radio (SDR) whose transmit (Tx) and receive (Rx) ports are connected to a UHF circulator and a voltage source that is controlled to output pulse-shaped bitstreams. The front-end is first directly wired to the third circulator port with an SMA cable. The SDR transmitter chain generates a CW at 913 MHz that excites the front-end through the circulator and the response is recorded by the SDR receiver chain. A bitstream of $N = 50$ b is generated and pulse shaped with an SRRC pulse with rolloff factor $\alpha = 0.5$ and filter delay $A = 6$. The values were selected for moderate mainlobe width (as a increases, the mainlobe becomes wider) and moderate filter length and sidelobe suppression (as A increases, the pulse becomes longer, but with a larger sidelobe suppression). The pulse train is normalized to the $[-1, 1]$ interval and is translated to the required bias voltage, using the $\hat{V}_{\text{bias}}(\hat{\Gamma})$ function (Fig. 18 for the p-i-n front-end). The SDR implements a receiver with SRRC matched filtering, bit-level synchronization, and symbol detection to verify the accurate reception of the bitstream. For wireless measurements, the front-end is detached from the circulator and is connected to a UHF antenna. The third port of the circulator is also connected to a UHF antenna for wireless transmission and reception from the SDR at the 900-MHz band.

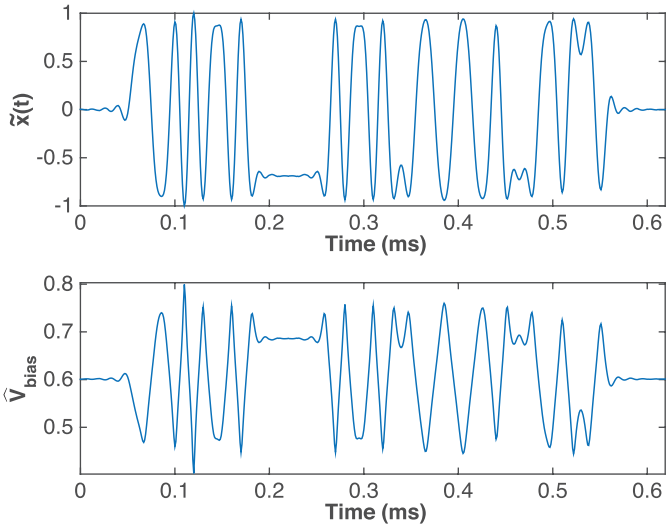

Fig. 18. 50-b SRRC-modulated waveform to be backscattered. Top: in reflection coefficient domain. Bottom: translated to bias voltage domain with measured p-i-n front-end data.

The wireless measurements have been conducted in an office environment with heavy multipath and clutter at 913 MHz with 2-dBi omnidirectional antennas for the reader and modulator, and carrier transmission power $P_T = 15$ dBm.

For comparison, a front-end consisting of a simple ON–OFF RF switch is tested with the same bitstream. In Fig. 19(a), the bitstream is shown, modulated with conventional rectangular pulses. In Fig. 19(b) and (c), the SDR-received backscattered SRRC pulses from the p-i-n front-end are shown for wired and wireless cases, respectively. The backscattered SRRC pulses are smooth, showcasing the continuity of $\Gamma(t)$ achieved with the p-i-n front-end, and are successfully decoded by the SDR receiver after matched filtering. In Fig. 19(d), the same bitstream with SRRC pulses is shown for the FET front-end.

In Fig. 20, the eye diagrams of the received SRRC waveforms are shown. The top eye diagram corresponds to an ideal

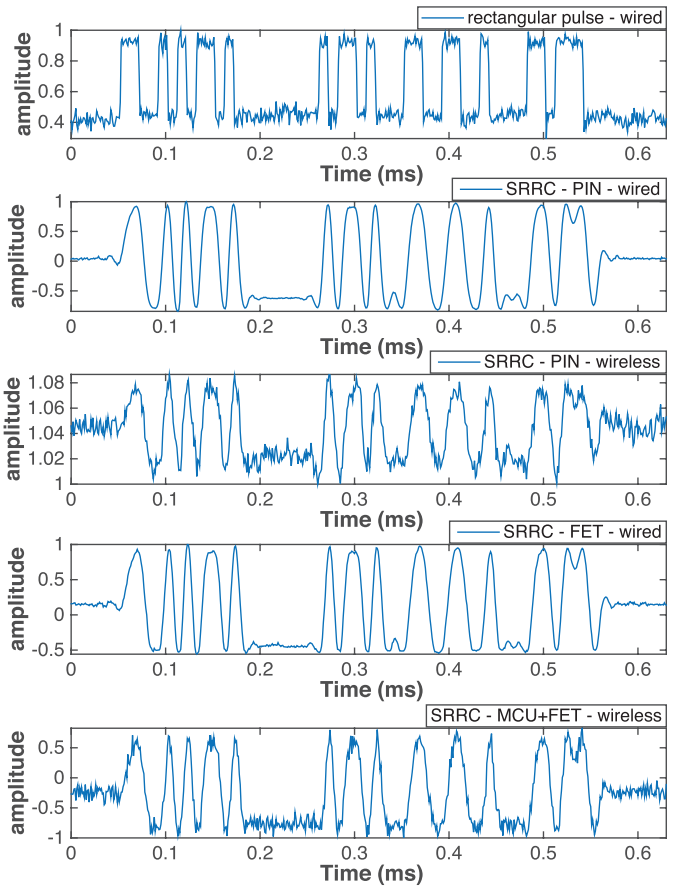

Fig. 19. SDR -measured backscatter signals in time domain. (a) Conventional rectangular pulses. (b), (c) SRRC pulses with p-i-n front-end. (d) SRRC pulses with FET front-end. (e) SRRC pulses with MCU + FET front-end.

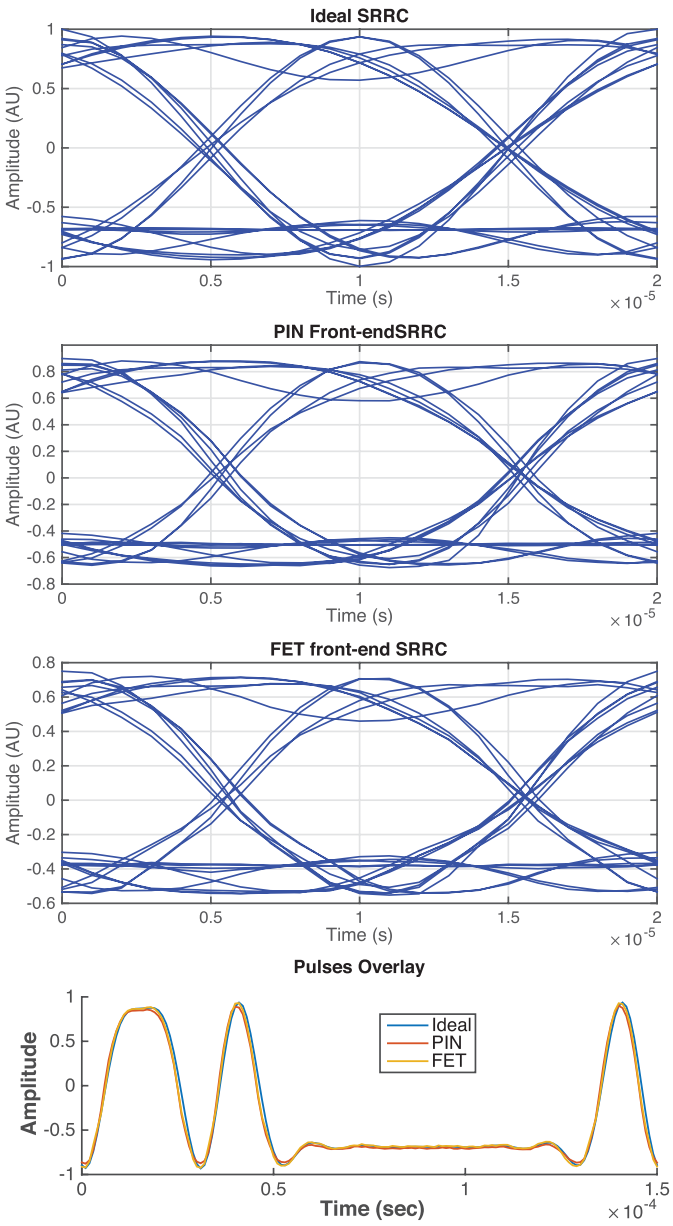

Fig. 20. Eye diagrams for SRRC pulse transmission and received pulses overlay for ideal SRRC, measured p-i-n-generated SRRC, and measured FET-generated SRRC.

(simulated) SRRC pulse train. The middle and bottom eye diagrams correspond to the p-i-n-generated and FET-generated SRRC pulse trains. It can be seen that the actual front-end backscattered pulses are closely following the envelope of the ideal SRRC pulses. The eye maximum height is equal to the magnitude of the difference of the reflection coefficient values at 0/1 V for the p-i-n front-end and 0/2 V for the FET front-end, respectively. The eye diagram is useful for quantifying the timing errors (jitter) of the pulse-shaped bits. The analyzed jitter percentage for the p-i-n front-end is 0.4%, and for the FET front-end, it is 0.35%. In Fig. 20(bottom), a portion of the SRRC-shaped pulsetrain is overlaid for the ideal case and the p-i-n and FET front-ends. It can be seen that the SRRC envelope is followed with minor variations, and most importantly, for the FET case, the effect of the curvature of $\Gamma(V_{\text{bias}})$ (Fig. 11) is negligible and has not affected the pulse shape. This verifies the accurate generation of the SRRC shape, without significant signal distortion.

The spectrum of the received rectangular pulse-modulated data is shown in Fig. 21 across with the spectrum of the SRRC-shaped data with the p-i-n front-end for a data rate of $R = 100$ kbits/s. It is apparent that the power decay is sharper for SRRC pulse-shaped backscatter, with an out-of-band suppression of up to 35 dB, for the same received pulse energy. Moreover, the SDR-captured spectrum of the SRRC pulse-shaped data occupies a frequency window of 150 kHz, which matches with the theoretical BW of SRRC $W = (1 + \alpha)R = 150$ kHz. It is noted that the spectrum around the second harmonic of the backscatter signal was monitored for reflected harmonics due to nonlinearity effects, but no increased power was observed.

In Fig. 22, the smoothed spectra of rectangular pulses, SRRC pulses from the p-i-n front-end, and SRRC pulses from the FET front-end are plotted for easy visual comparison. The two pulse-shaping front-ends feature an equal-width mainlobe, while the sidelobe suppression for the FET front-end is slightly higher (up to 42 dB) compared with the p-i-n front-end (up to 37 dB). The mainlobe of the pulse shaping front-ends' signals is narrower than the rectangular pulse one, and sidelobe suppression is around 40 dB with a fast decaying spectrum,

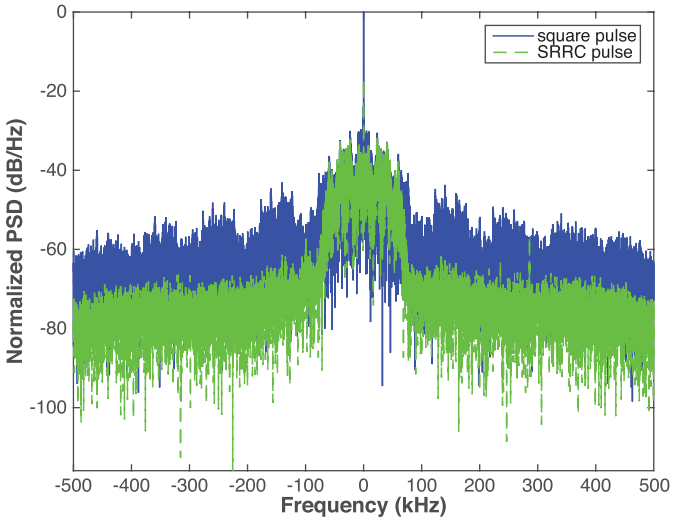

Fig. 21. Measured spectrum comparison of wireless SDR-received backscatter rectangular pulse and SRRC pulse-shaped backscatter. The strong dc peak corresponds to the reader's CW that illuminates the backscatter modulator.

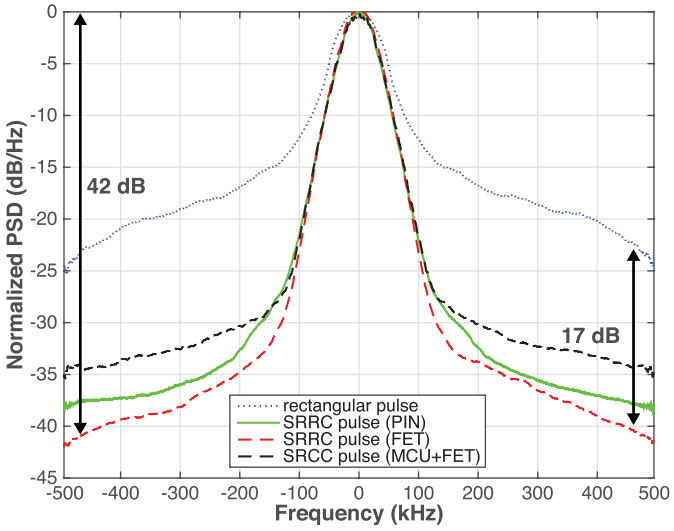

Fig. 22. Measured spectrum comparison of rectangular pulse-modulated waveform, SRRC pulse-shaped waveform from the p-i-n front-end, SRRC pulse-shaped waveform from the FET front-end, and SRRC pulse-shaped waveform from the FET driven by an MCU.

in contrast with a maximum suppression of 25 dB for the rectangular pulses and a slower decaying spectrum.

VII. Front-End Energy Efficiency

Backscatter modulators require very low energy for communication compared with active radio transmitters used for sensor networks. For example, active radios currently in the market, such as TI CC1101, Semtech SX1232, and Murata TRC103, which all operate in the UHF ISM band, feature power consumptions ranging from 48 to 375 mW, which correspond to required energy-per-bit ranging from 480 up to 3.75 μJ/bit for 100-kbit/s transmissions. On the other hand, backscatter modulators require significantly lower energy, due to their minimal RF front-end structure.

For power-limited scenarios, such as those commonly encountered in practical Internet-of-things sensors, it is necessary to compare backscatter front-ends with respect to power dissipation. However, since the purpose of a backscatter modulator is the communication with a reader/receiver, there are important communication parameters to be considered, such as the received SNR from a backscatter tag, the backscattered signal's BW, any signal energy losses associated with pulse shaping, and losses at the receiver's finite sampling rate/BW front-end. Energy per bit is not a sufficient metric for comparison for backscatter tags, because in backscatter modulation, the power dissipation of the front-end is not proportional to the transmitted signal's amplitude, as in active radios. In the latter, the dissipated front-end power is used toward the amplification of the RF signal that is *radiated* toward a receiver. At the receiver, the SNR is proportional to the received signal power, which is proportional to the radiated signal power, and therefore it is a function of the transmitter's dissipated power. In backscatter radio, the SNR at the reader is proportional to the received signal power, which is a function of the reflection coefficient values of the tag during its modulation states. Since for backscatter radio, the modulation takes place on the tag, whereas the carrier signal radiation takes place on a reader/carrier emitter/signal generator, the modulation front-end's efficiency characterization needs to involve both the power dissipation and the reflection coefficient values. This section describes a number of parameters that need to be specified for each front-end, and gives an *energy efficiency* metric formula for a fair comparison of front-ends under the same bitrate and finite receiver BW.

A. Energy Per Bit E_{bit}

The energy per bit E_{bit} of a backscatter modulator is the amount of energy required to be spent to backscatter 1 bit of information, regardless of the modulation scheme or constellation size. It is a direct function of the front-ends' power dissipation P_{dis} and the *bit* duration T_b (i.e., not symbol duration T_s)

$$E_{\text{bit}} = P_{\text{dis}} T_b \text{ (J/bit)} \tag{17}$$

where P_{dis} is in watts and T_b is in seconds/bit. For a binary modulation, the bit duration equals the symbol duration $T_b \equiv T_s$, but for higher order constellations, $T_s = T_b \log_2 M$, where M is the constellation order, e.g., for QPSK/4-QAM, $M = 4$ and the bit duration is half of the symbol duration.

For the p-i-n diode front-end of this paper, the *maximum* dissipation is $P_{\text{dis}} = 6$ mW, and for 100 kbits/s, $T_b = 10$ μs/bit; therefore, $E_{\text{bit}} = 60$ nJ/bit. Comparison can be made with the energy per bit of 400 nJ/bit for the 2× p-i-n QAM modulator of [16] in Table I.

For MOSFET circuits, the power dissipation can be calculated based on the supply voltage, gate leakage current, and switching dissipation. For the FET front-end of this paper, the *maximum* bias voltage is $V_{\max} = 2$ V, the gate leakage current and the gate capacitance are $I_{\text{GSS}} = 100$ nA and $C = 1$ pF, and the *maximum* switching speed for 100 kbits/s is $f_{\max} = 1/(2T_b) = 50$ kHz. Then the maximum power

TABLE I
BACKSCATTER FRONT-ENDS' COMPARISON. BITRATE: $R = 100$ kbits/s AND RECEIVER BW: $B = R/2$ (1 SAMPLE/BIT)

Front-end & modulation	Energy per bit (Power)	$\lvert\Delta\Gamma\rvert$	Pulse Energy Loss	Rx BW Energy Loss	Energy Efficiency	Signal Bandwidth
$2 \times$ PIN, 4-QAM, rect. pulses ([16])	800 nJ/bit (80 mW) (*)	0.44	0 dB	-1.1112 dB	52.7466 dB	∞
PIN, binary, SRRC pulses (this work)	$<$ 60 nJ/bit (6 mW)	1.8	-3.3475 dB	-0.4172 dB	$>$ 73.5681 dB	75 kHz
SP4T, 4-QAM, rect. pulses ([11])	14.037 pJ/bit (1.405 μW) (*)	≤ 1.55 (#)	0 dB	-0.4389 dB	111.8916 dB	∞
FET, binary, rect. pulses (this work)	$<$ 3 pJ/bit (300 nW)	1.5	0 dB	-1.1112 dB	$>$ 117.6487 dB	∞
FET, binary, SRRC pulses (this work)	$<$ 3 pJ/bit (300 nW)	1.5	-3.3475 dB	-0.4172 dB	$>$ 114.9947 dB	75 kHz
FET, 4-PAM, rect. pulses (this work)	$<$ 2.5 pJ/bit (250 nW)	1.5	0 dB	-0.4421 dB	$>$ 119.1004 dB	∞
FET, 4-PAM, SRRC pulses (this work)	$<$ 2.5 pJ/bit (250 nW)	1.5	-3.2905 dB	0 dB	$>$ 116.2359 dB	37.5 kHz

* Average power consumption is assumed
# Calculated from the manufacturer-provided insertion loss in SP4T datasheet [24] and does not include additional losses; all other rows include measured transmission line and connectors losses.

dissipation can be calculated as

$$P_{\text{dis}} < I_{\text{GSS}} V_{\max} + \frac{1}{2} C V_{\max}^2 f_{\max} = 300 \text{ nW} \tag{18}$$

and $E_{\text{bit}} < 3$ pJ/bit. For implementing 4-PAM with the same FET front-end, the symbol duration is $T_s = 2T_b$, and therefore the switching speed reduces to 25 kHz. Then the power dissipation is $P_{\text{dis}} < 250$ nW and $E_{\text{bit}} < 2.5$ pJ/bit.

B. Average Reflected Power $|\Delta\Gamma|^2$

It is known that the detection error at the reader in terms of bit error rate (BER) is minimized when the received SNR is maximized for the backscattered signal. From [18], [25], and [19], the SNR for binary backscatter modulators is proportional to

$$|\Delta\Gamma|^2 \triangleq |\Gamma_1 - \Gamma_0|^2 \tag{19}$$

where Γ_0 and Γ_1 are the two reflection coefficient values corresponding to the two discrete load values used for modulation and $\Delta\Gamma$ denotes their difference. The difference amplitude $|\Delta\Gamma|$ has to be maximized, in order to minimize the BER at the reader. This means that the distance between the two discrete constellation points Γ_0 and Γ_1 on the Smith chart has to be maximized. For pulse shaping backscatter front-ends, the difference amplitude is defined as $|\Delta\Gamma_{\text{ps}}|^2 \triangleq |\Gamma(V_{\min}) - \Gamma(V_{\max})|^2$. A large $|\Delta\Gamma_{\text{ps}}|$ means a large distance on the complex plane between a positive pulse's peak value and a negative pulse's peak value. This is analogous to the maximization of $|\Delta\Gamma|$ for conventional backscatter modulators and leads to lower BER for pulse-shaped backscatter. For the p-i-n diode front-end, $|\Delta\Gamma| \approx 1.8$, while for the FET front-end, $|\Delta\Gamma| \approx 1.5$. Comparison of other front-ends $|\Delta\Gamma|$ can be seen in Table I, where the $|\Delta\Gamma|$ shown for the p-i-n and SP4T QAM modulators corresponds to the difference between two antipodal points on the Smith chart, although the $|\Delta\Gamma|$ between two adjacent points is less than that.

C. Pulse Energy Loss

Typical backscatter modulators have $|\Gamma| \leq 1$, which means that the reflected signal amplitude is limited to a maximum value of 1. In the ideal case, a rectangular pulse modulator with states $\Gamma_0 = 1$ and $\Gamma_1 = -1$ will be fully reflective for the whole duration of the signal $\tilde{x}(t)$, maximizing the signal energy

$$E_x^{\text{rect}} = \int_{-\infty}^{+\infty} |\tilde{x}_{\text{rect}}|^2 \, dt \tag{20}$$

which maximizes the signal SNR at the reader. When performing pulse shaping with nonrectangular pulses though, a nonrectangular signal with a maximum amplitude of 1 will have energy

$$E_x^{\text{pulse}} = \int_{-\infty}^{+\infty} |\tilde{x}_{\text{pulse}}|^2 \, dt \tag{21}$$

which is always be less than E_x^{rect}. The ratio

$$L_{\text{pulse}} = E_x^{\text{pulse}} / E_x^{\text{rect}} \tag{22}$$

is the *pulse energy loss*, and it can be calculated numerically or experimentally by generating very long sequences of bits and calculating their energy in the time domain. As an example, the calculated pulse energy loss for binary modulation with SRRC pulse shaping compared with rectangular pulses is $L_{\text{pulse}} \approx -3.35$ dB. For 4-PAM modulation with SRRC pulses, the loss is $L_{\text{pulse}} \approx -3.29$ dB (Table I).

D. Receiver Bandwidth (Rx BW) Energy Loss

Receiver chains in readers have a finite BW defined by the sampling rate F_s of the receiver. The baseband Rx BW is $B = F_s/2$, and thus the received signal spectrum at the receiver is in the $-B \leq F \leq B$ frequency band. Depending on the backscattered signal characteristics (i.e., the pulse shape) the full signal PSD cannot be represented within the receiver BW. Since ideal receivers with infinite BW do not exist in practice (and if they did, the additive noise power at the receiver would be infinite), it is imperative to compare the signal energy loss due to Rx BW finiteness. This is performed under a reference unit BW for all signals, regardless of the total BW they need to be fully represented. Choosing $F_s = R$, exactly 1 sample/bit is acquired at the receiver within the unit BW $B = R/2$. The Rx BW energy loss is defined as

$$L_{\text{BW}} = \frac{\int_{-B}^{B} |\tilde{X}_{\text{pulse}}(f)|^2 \, dF}{\int_{-\infty}^{\infty} |\tilde{X}_{\text{pulse}}(f)|^2 \, dF} \tag{23}$$

and can be calculated (or approximated) numerically by computing $\tilde{X}(f)$, the Fourier transform of $\tilde{x}_{\text{pulse}}(t)$, for any pulse shape. As an example, the Rx BW energy loss for binary modulation with rectangular pulses is $L_{\text{BW}} \approx -1.11$ dB, while for binary modulation with SRRC pulses, it is $L_{\text{BW}} \approx -0.41$ dB. This is intuitive, due to the higher spectral efficiency of SRRC pulses compared with rectangular pulses. Other calculated Rx BW energy loss values can be seen in Table I, where interesting comparisons can be made between different modulation schemes and pulse shapes.

E. Energy Efficiency

An *energy efficiency* metric shall be defined that involves a front-end's energy per bit and reflected power capability, as well as the respective pulse energy loss and Rx BW energy loss

$$e = \frac{|\Delta\Gamma|^2}{E_{\text{bit}}} L_{\text{pulse}}\ L_{\text{BW}}\ \text{(bits/J)}. \tag{24}$$

The formula intuitively expresses how much the energy spent for each bit is worth in terms of useful signal SNR at the reader. It takes into account the modulation scheme, constellation size, pulse shape, finite Rx BW, and the front-end circuit implementation. The formula can be fairly used for direct comparisons between front-ends as in Table I, where the increased efficiency of each front-end can be seen.

It is shown that for a constellation size of $M = 4$, this paper's front-end with binary modulation has an increased energy efficiency when compared with the two 4-QAM front-ends of the same data rate, with or without SRRC pulse shaping. For the FET front-end, when binary modulation and SRRC pulse shaping are used, the energy efficiency is 2.5 dB lower compared with using the same FET with rectangular pulses. This is mainly due to the pulse energy loss, but comes at the benefit of a significantly reduced BW of 75 kHz, compared with the infinite rectangular pulses BW. The FET front-end shows an increased performance with higher order constellations, e.g., compared with the SP4T 4-QAM front-end, it is 7.2 dB more efficient with rectangular 4-PAM, and 4.33 dB more energy efficient with SRRC-shaped 4-PAM, while also featuring a reduced signal BW of 37.5 kHz. From these results, it can be derived that the FET pulse shaping front-end would be favorable to use for power-limited and BW-limited systems.

F. Link Budgets

The received power from a pulse shaping modulator can be calculated with [25]

$$P_R = P_T \frac{G_T G_R G_{\text{tag}}^2 \lambda^4}{(4\pi)^4 r_T^2 r_R^2} \frac{|\Delta\Gamma|^2}{4} \tag{25}$$

where G_T and G_R are the gains of the reader transmit and receive antennas, G_{tag} is the gain of the tag antenna, $\lambda = c/f_c$ is the wavelength, and r_T and r_T are the distance between the transmitter and tag and the distance between the tag and receiver, respectively. For a monostatic reader, $G_R = G_T$ and $r_T = r_R$. The received SNR from a pulse shaping modulator is

$$\text{SNR} = \frac{P_R\ K}{N_F\ N_0\ B} L_{\text{pulse}}\ L_{\text{BW}} \tag{26}$$

where $N_0 = -174$ dBm/Hz is the noise PSD, $K \triangleq F_s/R$ is the number of received samples/bit (oversampling factor), B is the receiver BW, and N_F is the receiver noise figure.

For the FET modulator of this paper performing binary modulation with SRRC shaping, a maximum communication range can be found for $|\Delta\Gamma| = 1.5$, $P_T = 15$ dBm (SDR output power), $N_F = 10$ dB, $B = 500$ kHz ($K = 10$ samples/bit), $G_T = G_R = G_{\text{tag}} = 2.15$ dBi, and $f_c = 913$ MHz. The threshold is set to a high SNR value of 10 dB, to achieve a minor BER value of 10^{-5} ([1]), which gives a maximum monostatic range of 45 m. However, utilizing bistatic architectures the tag-to-receiver distance can be boosted to 100+ m [7], [9].

VIII. Practical MCU Implementation

To demonstrate the feasibility of generating arbitrary waveforms and perform pulse shaping on low computational power platforms, the backscatter communication block in Fig. 12 has been ported on an off-the-shelf MCU board as a proof of concept. The Silicon Labs C8051F120 MCU has been utilized, with a typical current consumption of 2.431 mA at 3 V, with a system clock of 3.0625 MHz [26]. The F120 incorporates a 12-bit digital-to-analog converter (DAC) that is capable of generating arbitrary waveforms with a typical current consumption of 110 μA, which corresponds to a 4.5% power consumption increase for the MCU. Although the F120 MCU has been used as an example, other lower consumption commercial MCUs can be utilized with the same principles.

The MCU has been set up to output 50-bit SRRC-shaped bitstreams at 100 kbits/s, translated to output voltage levels that are routed to the DAC unit. The DAC output terminal drives the BF1118 FET transistor front-end, and the MCU effectively replaces the V-source block in Fig. 17. A photo of the Silicon Labs development kit and the front-end can be seen in Fig. 23. It is noted that no other peripherals on the board are utilized (e.g., serial transceiver IC, external crystal oscillator, etc.), and therefore the system can be implemented on a single board hosting only the MCU, the FET front-end, and a connector for the JTAG programming pins and power pins, where a 3 V coin cell battery holder, or a solar cell, or a harvester's output port can be interfaced.

The wirelessly received waveform of the MCU-modulated data can be seen in Fig. 19(e) for comparison with the other SDR-received waveforms. The SDR-received spectrum of the FET front-end driven by the MCU can be seen in Fig. 22, where a sidelobe suppression of up to 35 dB is achieved. This can be further improved with the utilization of a higher resolution DAC; detailed information on optimized DAC operation and how quantization (bit resolution) affects the signal spectrum can be found in several publications and whitepapers (see [27]–[29]). The DAC utilized for this paper as a proof of concept has a resolution of 12 bits, a typical

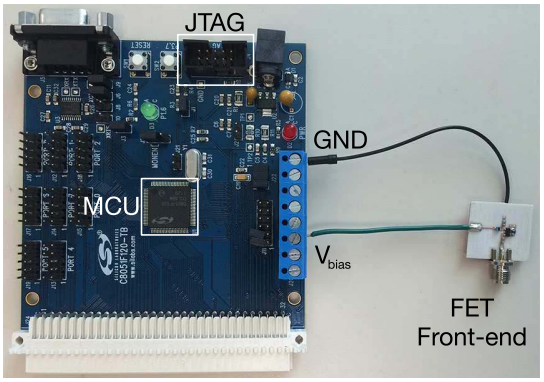

Fig. 23. Pulse-shaping FET front-end interfaced to MCU board. Only the MCU and JTAG programming connector are utilized from the development kit.

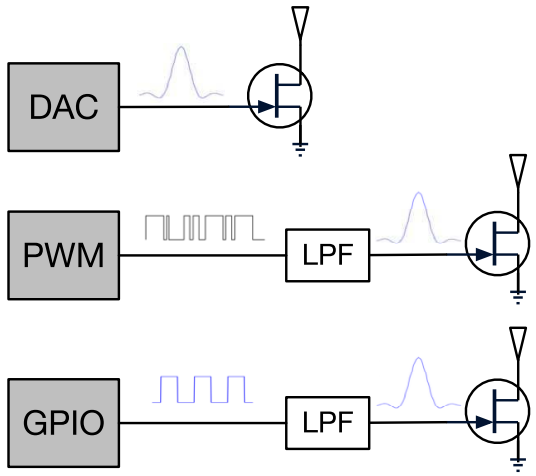

Fig. 24. Pulse-shaping implementation options.

power consumption of 110 μA, and a slew rate of 0.44 V/μs for a 40-pF load, which is more than adequate for the FET modulator since the load (FET gate) capacitance is $1 \ll 40$ pF and no sharp transitions from a full-OFF (0 V) to full-ON (2 V) level are required. The transitions are always slower than $f_{\max} = 1/(2T_{\text{bit}}) = 50$ kHz and would require in maximum a slew rate of $V_{\max}/(2T_b) = 2$ V/20 μs $= 0.1$ V/μs.

Another option for generating analog signals involves the pulsewidth modulator (PWM) unit available on many MCUs. A PWM outputs pulses of variable width that can be filtered with a low-pass network to generate analog waveforms. The implementation details are MCU specific, but examples can be found in [30]–[33]. The main challenge with this approach is the design of the filter in terms of sharp cutoff (dB/octave) and in-band signal attenuation.

An even more minimal approach for pulse shaping can be the utilization of a fully passive RLC low-pass network to filter rectangular pulse-modulated bitstreams as they come out of a tag's digital port and before they drive the backscatter modulator. For example, Gaussian pulse shaping could be achieved by constructing an LC low-pass Gaussian filter to suppress the high-frequency components of rectangular pulses that drive the front-end's transistor [34], [35]. The main limitation with this approach is that the pulse shape is 'hardcoded' in the circuit, and thus no arbitrary waveforms can be generated; despite that, it can be an appealing practical implementation for non-MCU tags, such as the ones in [36] and [23], where the only option is to switch between two impedance states and no DACs or PWMs are available. The complexity reduction by removing the need of a DAC or PWM comes at the cost of increased signal processing at the reader, e.g., in the case that Gaussian filters are implemented, the pulse-shaped bitstreams will suffer from ISI. Moreover, due to the fact that in general there is no linear relationship between the bias voltage $V_{\text{bias}}(t)$ and the reflection coefficient $\Gamma(t)$, the backscattered pulses will be distorted, which translates in additional signal processing steps at the reader (equalization), as well as undesired increase of the pulses' BW.

The three options for implementing pulse shaping on a tag are summarized in Fig. 24. The first (DAC) is the most flexible in terms of arbitrary signal generation, while the last (passive LPF at a digital general purpose IO pin of an MCU) gives the less flexibility, but lowest complexity and power consumption.

IX. Conclusion

An extensive presentation was given of the concepts behind backscatter pulse shaping, along with the signal processing and the front-end implementations to achieve it. The principle of continuously varying the tag reflection coefficient and how this translates to pulse-shaped backscatter signals was analyzed and demonstrated with very low complexity front-ends that utilize a single nonlinear component, e.g., a p-i-n diode or a FET transistor. Despite the front-ends' low complexity and minimized energy footprint, they can effectively break the limitations of rectangular waveforms and high BW occupancy found in conventional RFID tags. SRRC pulses were created and backscattered as a proof of concept, but other arbitrary pulses can be generated as well. Tags can essentially become miniature SDRs to implement diverse communication schemes, spectral characteristics, or modulation formats. This paper has offered a missing piece to complete backscatter radio as a communication scheme for low-complexity low-energy sensor tags and computational RFID.

References

[1] J. G. Proakis, *Digital Communications*, 4th ed. New York, NY, USA: McGraw-Hill, 2001.

[2] S. J. Maeng and B. G. Lee, "A design of linear-phased IIR Nyquist filters," *IEEE J. Sel. Areas Commun.*, vol. 13, no. 1, pp. 167–175, Jan. 1995.

[3] D. M. Dobkin, *The RF in RFID: Passive UHF RFID in Practice*. Newton, MA, USA: Elsevier, 2008.

[4] A. P. Sample, D. J. Yeager, P. S. Powledge, and J. R. Smith, "Design of a passively-powered, programmable sensing platform for UHF RFID systems," in *Proc. IEEE Int. Conf. RFID*, Mar. 2007, pp. 149–156.

[5] *EPC Radio-Frequency Identity Protocols, Class-1 Generation-2 UHF RFID Protocol for Communications at 860MHz–960MHz, Version 1.2.0*, EPC Global, 2008.

[6] J. Kimionis, A. Bletsas, and J. N. Sahalos, "Design and implementation of RFID systems with software defined radio," in *Proc. 6th Eur. Conf. Antennas Propag. (EUCAP)*, Mar. 2012, pp. 3464–3468.

[7] G. Vougioukas, S.-N. Daskalakis, and A. Bletsas, "Could battery-less scatter radio tags achieve 270-meter range?" in *Proc. IEEE Wireless Power Transf. Conf.*, Aveiro, Portugal, May 2016, pp. 1–3.
[8] J. Kimionis, A. Bletsas, and J. N. Sahalos, "Bistatic backscatter radio for tag read-range extension," in *Proc. IEEE Int. Conf. RFID-Technol. Appl. (RFID-TA)*, Nice, France, Nov. 2012, pp. 356–361.
[9] J. Kimionis, A. Bletsas, and J. N. Sahalos, "Increased range bistatic scatter radio," *IEEE Trans. Commun.*, vol. 62, no. 3, pp. 1091–1104, Mar. 2014.
[10] V. Liu, A. Parks, V. Talla, S. Gollakota, D. Wetherall, and J. R. Smith, "Ambient backscatter: Wireless communication out of thin air," in *Proc. ACM SIGCOMM Conf. (SIGCOMM)*, Hong Kong, 2013, pp. 39–50.
[11] S. J. Thomas, E. Wheeler, J. Teizer, and M. S. Reynolds, "Quadrature amplitude modulated backscatter in passive and semipassive UHF RFID systems," *IEEE Trans. Microw. Theory Techn.*, vol. 60, no. 4, pp. 1175–1182, Apr. 2012.
[12] R. Correia and N. B. Carvalho, "Design of high order modulation backscatter wireless sensor for passive IoT solutions," in *Proc. IEEE Wireless Power Transf. Conf.*, Aveiro, Portugal, May 2016, pp. 1–3.
[13] Y. Ma, X. Hui, and E. C. Kan, "Harmonic-WISP: A passive broadband harmonic RFID platform," in *IEEE MTT-S Int. Microw. Symp. Dig.*, San Francisco, CA, USA, May 2016, pp. 1–4.
[14] J. Kimionis and M. M. Tentzeris, "Software-defined reader for multimodal RFID sensing," in *IEEE MTT-S Int. Microw. Symp. Dig.*, San Francisco, CA, USA, May 2016, pp. 1–4.
[15] Y. Taur and T. H. Ning, *Fundamentals of Modern VLSI Devices*, 2nd ed. Cambridge, U.K.: Cambridge Univ., 2013.
[16] M. Winkler, T. Faseth, H. Arthaber, and G. Magerl, "An UHF RFID tag emulator for precise emulation of the physical layer," in *Proc. Eur. Wireless Technol. Conf. (EuWIT)*, Paris, France, Sep. 2010, pp. 273–276.
[17] V. Viikari, J. Chisum, and H. Seppa, "Wireless passive photo detector for insect tracking," *Microw. Opt. Technol. Lett.*, vol. 52, no. 10, pp. 2312–2315, Jul. 2010.
[18] F. Fuschini, C. Piersanti, F. Paolazzi, and G. Falciasecca, "Analytical approach to the backscattering from UHF RFID transponder," *IEEE Antennas Wireless Propag. Lett.*, vol. 7, pp. 33–35, Feb. 2008.
[19] A. Bletsas, A. G. Dimitriou, and J. N. Sahalos, "Improving backscatter radio tag efficiency," *IEEE Trans. Microw. Theory Techn.*, vol. 58, no. 6, pp. 1502–1509, Jun. 2010.
[20] N. S. Alagha and P. Kabal, "Generalized raised-cosine filters," *IEEE Trans. Commun.*, vol. 47, no. 7, pp. 989–997, Jul. 1999.
[21] J. Kimionis, A. Georgiadis, A. Collado, and M. M. Tentzeris, "Enhancement of RF tag backscatter efficiency with low-power reflection amplifiers," *IEEE Trans. Microw. Theory Techn.*, vol. 62, no. 12, pp. 3562–3571, Dec. 2014.
[22] J. Kimionis and M. M. Tentzeris, "RF tag front-end design for uncompromised communication and harvesting," in *Proc. IEEE RFID Technol. Appl. Conf. (RFID-TA)*, Tampere, Finland, Sep. 2014, pp. 109–114.
[23] E. Kampianakis, J. Kimionis, K. Tountas, C. Konstantopoulos, E. Koutroulis, and A. Bletsas, "Wireless environmental sensor networking with analog scatter radio and timer principles," *IEEE Sensors J.*, vol. 14, no. 10, pp. 3365–3376, Oct. 2014.
[24] *ADG904 4:1 Mux/SP4T, Datasheet*, Analog Devices, Norwood, MA, USA, 2013.
[25] J. D. Griffin and G. D. Durgin, "Complete link budgets for backscatter-radio and RFID systems," *IEEE Antennas Propag. Mag.*, vol. 51, no. 2, pp. 11–25, Feb. 2009.
[26] *C8051F12x and C8051F13x Mixed-Signal ISP Flash MCU Family, Datasheet*, Silicon Labs, Austin, TX, USA, 2003.
[27] "Understanding data converters," Texas Instrum., Dallas, TX, USA, Tech. Rep. SLAA013, 1995.
[28] P. Xiao, C. Toal, D. Burns, V. Fusco, and C. Cowan, "Transmit and receive filter design for OFDM based WLAN systems," in *Proc. Int. Conf. Wireless Commun. Signal Process.*, vol. 1. Oct. 2010, pp. 1–4.
[29] V. Agarwal, P. Kim, D.-G. Oh, and D.-S. Ahn, "Hardware efficient root-raised-cosine pulse shaping filter for DVB-S2 receivers," in *Advances in Computing and Communications*, A. Abraham, J. L. Mauri, J. F. Buford, J. Suzuki, and S. M. Thampi, Eds. Berlin, Germany: Springer, 2011, pp. 595–603.
[30] M. Mitchell, "Using PWM timer_B as a DAC," Texas Instrum., Dallas, TX, USA, Appl. Rep. SLAA116, Dec. 2000.
[31] "16-bit PWM using an on-chip timer," Silicon Labs, Austin, TX, USA, Appl. Note AN110, Dec. 2003.
[32] D. M. Alter, "Using PWM output as a digital-to-analog converter on a TMS320F280x digital signal controller," Texas Instrum., Dallas, TX, USA, App. Rep. SPRAA88A, Sep. 2008.
[33] R. Metivier, "Method for converting a PWM output to an analog output when using Hall-effect sensor ICs," Allegro Microsyst., LLC, Worcester, MA, USA, Appl. Note 296094-AN, 2013.
[34] L. Besser and R. Gilmore, *Practical RF Circuit Design for Modern Wireless Systems*, vol. 2. Norwood, MA, USA: Artech House, 2003.
[35] J.-S. G. Hong and M. J. Lancaster, *Microstrip Filters for RF/Microwave Applications*. Hoboken, NJ, USA: Wiley, 2004.
[36] A. Strobel, C. Carlowitz, R. Wolf, F. Ellinger, and M. Vossiek, "A millimeter-wave low-power active backscatter tag for FMCW radar systems," *IEEE Trans. Microw. Theory Techn.*, vol. 61, no. 5, pp. 1964–1972, May 2013.

John Kimionis (S'10) received the Diploma degree and M.Sc. degree in electronic and computer engineering from the Technical University of Crete, Chania, Greece, in 2011 and 2013, respectively, where he was with the Telecom Lab.

He is currently a Ph.D. candidate with the School of Electrical and Computer Engineering, Georgia Institute of Technology, Atlanta, GA, USA, and a Research Assistant with the ATHENA Group. His research interests are in the areas of spectral-efficient and energy-efficient backscatter radio and RFID, software-defined radio for sensor networks, RF front-end design for wireless sensors, and additive manufacturing techniques.

Mr. Kimionis was the recipient of fellowship awards for his undergraduate and graduate studies and he is a Texas Instruments Scholar for his mentoring service for the Opportunity Research Scholars (ORS) program at the Georgia Insitute of Technology. He was the recipient of IEEE student travel grants, the First Best Student Paper Award of the IEEE International Conference on RFID-Technologies and Applications (RFID-TA) 2014, Tampere, Finland, as well as the Second Best Student Paper Award of the IEEE International Conference on RFID-Technologies and Applications (RFID-TA) 2011, Sitges, Barcelona, Spain. He has been a member of the IEEE Microwave Theory and Techniques Society, the IEEE Communications Society, and a board member of the IEEE MTT-24 RFID Technologies Committee.

Manos M. Tentzeris (S'89–M'92–SM'03–F'10) received the Diploma degree (*magna cum laude*) in electrical and computer engineering from the National Technical University of Athens, Athens, Greece, and the M.S. and Ph.D. degrees in electrical engineering and computer science from the University of Michigan, Ann Arbor, MI, USA.

He has served as the Head of the Georgia Tech Electrical and Computer Engineering Electromagnetics Technical Interest Group at the Georgia Institute of Technology, Atlanta, GA, USA, as an Associate Director for RFID/Sensors research at the Georgia Electronic Design Center, Atlanta, and as an Associate Director for RF Research at the GT NSF-Packaging Research Center, where he was also the RF Alliance Leader. He was a Visiting Professor with the Technical University of Munich, Munich, Germany, in 2002, a Visiting Professor with GTRI-Ireland, Athlone, Ireland, in 2009, and a Visiting Professor with LAAS-CNRS, Toulouse, France, in 2010. He is currently a Ken Byers Professor of flexible electronics with the School of Electrical and Computer Engineering, Georgia Institute of Technology. He is the Head of the Athena research group (20 researchers). He has authored more than 620 papers in refereed journals and conference proceedings, five books, and 25 book chapters. He has helped to develop academic programs in 3-D/inkjet-printed RF electronics and modules, flexible electronics, origami and morphing electromagnetics, highly integrated/multilayer packaging for RF and wireless applications using ceramic and organic flexible materials, paper-based RFID's and sensors, wireless sensors and biosensors, wearable electronics, "Green" electronics, energy harvesting and wireless power transfer, nanotechnology applications in RF, Microwave MEM's, and SOP-integrated (UWB, multiband, mmW, and conformal) antennas.

Dr. Tentzeris was a recipient/corecipient of the 2015 IET Microwaves, Antennas, and Propagation Premium Award, the 2014 Georgia Tech ECE Distinguished Faculty Achievement Award, the 2014 IEEE RFID-TA Best Student Paper Award, the 2013 *IET Microwaves, Antennas, and Propagation* Premium Award, the 2012 FiDiPro Award in Finland, the iCMG Architecture Award of Excellence, the 2010 IEEE Antennas and Propagation Society Piergiorgio L. E. Uslenghi Letters Prize Paper Award, the 2011 International Workshop on Structural Health Monitoring Best Student Paper Award, the 2010 Georgia Tech Senior Faculty Outstanding Undergraduate Research Mentor Award, the 2009 IEEE TRANSACTIONS ON COMPONENTS AND PACKAGING TECHNOLOGIES Best Paper Award, the 2009 E.T.S.Walton Award from the Irish Science Foundation, the 2007 IEEE APS Symposium Best Student Paper Award, the 2007 IEEE IMS Third Best Student Paper Award, the 2007 ISAP 2007 Poster Presentation Award, the 2006 IEEE MTT Outstanding Young Engineer Award, the 2006 Asian-Pacific Microwave Conference Award, the 2004 IEEE TRANSACTIONS ON ADVANCED PACKAGING Commendable Paper Award, the 2003 NASA Godfrey "Art" Anzic Collaborative Distinguished Publication Award, the 2003 IBC International Educator of the Year Award, the 2003 IEEE CPMT Outstanding Young Engineer Award, the 2002 International Conference on Microwave and Millimeter-Wave Technology Best Paper Award (Beijing, China), the 2002 Georgia Tech-ECE Outstanding Junior Faculty Award, the 2001 ACES Conference Best Paper Award, the 2000 NSF CAREER Award, and the 1997 Best Paper Award of the International hybrid Microelectronics and Packaging Society. He was the TPC Chair for the IEEE IMS 2008 Symposium and the Chair of the 2005 IEEE CEM-TD Workshop and is the Vice-Chair of the RF Technical Committee (TC16) of the IEEE CPMT Society. He served as one of the IEEE MTT-S Distinguished Microwave Lecturers from 2010 to 2012 and is one of the IEEE CRFID Distinguished Lecturers. He is the Founder and has served as the Chair of the RFID Technical Committee (TC24) of the IEEE MTT Society and is the Secretary/Treasurer of the IEEE C-RFID. He has served as the Associate Editor of the IEEE TRANSACTIONS ON MICROWAVE THEORY AND TECHNIQUES, the IEEE TRANSACTIONS ON ADVANCED PACKAGING, and the *International Journal on Antennas and Propagation*. He has given more than 100 invited talks to various universities and companies all over the world. He is a member of the URSI-Commission D, a member of the MTT-15 Committee, an Associate Member of EuMA, a fellow of the Electromagnetic Academy, and a member of the Technical Chamber of Greece.